Imaging the Surface of Altair

John D. Monnier, *et al.*

Science **317**, 342 (2007);
DOI: 10.1126/science.1143205

current data set confirmed extensive haplotype sharing of up to 600 kb around *FRI* (fig. S15), as well as haplotype sharing around other low-frequency candidate alleles (*36*) (fig. S16).

We looked for evidence of additional sweeps in the form of extensive haplotype sharing across at least 50 kb (Fig. 5 and figs. S17 to S19). Because of its composition and size, our sample is only suited for discovering species-wide sweeps. We did not find evidence of a recent sweep affecting all accessions. However, on chromosome 1 all but two accessions were nearly identical for approximately 500 kb (Fig. 5). The two unaffected accessions, Cvi-0 and Lov-5, are from the periphery of the *A. thaliana* range and may have escaped the sweep because of different selective environments or geographic isolation. The region of most extreme haplotype sharing extends from 20.34 to 20.49 Mb and contains 50 annotated genes (table S13). There are several additional candidates for sweeps affecting a smaller number of accessions (figs. S17 to S20). With the SNPs identified in this project and the ability to determine their frequencies in hundreds to thousands of accessions (*37*), the goal of understanding the forces shaping diversity at global, regional, and local scales will soon be within reach.

Conclusions. We used array-based methods to generate a comprehensive polymorphism resource for *A. thaliana*. Our SNP data set is highly applicable for linkage disequilibrium mapping studies. In addition, we identified hundreds of thousands of polymorphisms in both coding and noncoding regions, providing an important resource for both evolutionary genetic and functional studies. Recently, studies in plants with large, repetitive genomes, like maize (genome size ~2.5 Gb), have shown that as much as 50% of sequences can differ between strains (*38*). In contrast to these plants, *A. thaliana* has a compact genome consisting largely of unique sequences. Nevertheless, our data highlight that even for species with streamlined genomes, individuals can differ substantially in genic content.

Mutations identified in laboratory phenotypic screens typically have marked phenotypic effects that are likely detrimental in the wild. The genes segregating for major-effect changes in our population have few known mutant phenotypes (tables S10 and S11), but nonetheless, allele frequency patterns suggest functional constraints under natural conditions. Variation in copy number for genic sequences may explain this observation; in a given accession, higher constraint may be observed if a paralog is absent. Nevertheless, as highlighted by the current study, many genes harboring major-effect changes in wild populations are likely to mediate interactions with the environment. Ultimately, experiments under more natural conditions will be required to fully appreciate the functional relevance of such sequence variation.

References and Notes

1. The International HapMap Consortium, *Nature* **437**, 1299 (2005).
2. J. Kling, *Nat. Biotechnol.* **23**, 1333 (2005).
3. D. A. Hinds *et al.*, *Science* **307**, 1072 (2005).
4. N. Patil *et al.*, *Science* **294**, 1719 (2001).
5. The Arabidopsis Genome Initiative, *Nature* **408**, 796 (2000).
6. M. Nordborg *et al.*, *PLoS Biol.* **3**, e196 (2005).
7. Materials and methods are available as supporting material on *Science* Online.
8. B. Schölkopf, A. Smola, *Learning with Kernels* (MIT Press, Cambridge, MA, 2002).
9. V. N. Vapnik, *Estimation of Dependences Based on Emperical Data* (Springer, New York, 1982; reprinted by Springer, New York, 2006).
10. SNP and PRP data sets along with effects on genes and pseudochromosome sequences are hosted at The *Arabidopsis* Information Resource (TAIR) (www.arabidopsis.org/).
11. D. A. Hinds, A. P. Kloek, M. Jen, X. Chen, K. A. Frazer, *Nat. Genet.* **38**, 82 (2006).
12. TAIR annotation Version 6 (www.ncbi.nlm.nih.gov/mapview/map_search.cgi?taxid=3702).
13. G. A. Tuskan *et al.*, *Science* **313**, 1596 (2006).
14. M. Lynch, J. S. Conery, *Science* **290**, 1151 (2000).
15. G. Blanc, K. Hokamp, K. H. Wolfe, *Genome Res.* **13**, 137 (2003).
16. J. D. Jones, J. L. Dangl, *Nature* **444**, 323 (2006).
17. E. G. Bakker, C. Toomajian, M. Kreitman, J. Bergelson, *Plant Cell* **18**, 1803 (2006).
18. M. R. Grant *et al.*, *Proc. Natl. Acad. Sci. U.S.A.* **95**, 15843 (1998).
19. J. Shen, H. Araki, L. Chen, J. Q. Chen, D. Tian, *Genetics* **172**, 1243 (2006).
20. S. H. Shiu, A. B. Bleecker, *Sci. STKE* **2001**, RE22 (2001).
21. W. Y. Song *et al.*, *Science* **270**, 1804 (1995).
22. E. A. Stahl, G. Dwyer, R. Mauricio, M. Kreitman, J. Bergelson, *Nature* **400**, 667 (1999).
23. E. Lechner, P. Achard, A. Vansiri, T. Potuschak, P. Genschik, *Curr. Opin. Plant Biol.* **9**, 631 (2006).
24. J. H. Thomas, *Genome Res.* **16**, 1017 (2006).
25. B. C. Meyers, A. Kozik, A. Griego, H. Kuang, R. W. Michelmore, *Plant Cell* **15**, 809 (2003).
26. K. J. Schmid, S. Ramos-Onsins, H. Ringys-Beckstein, B. Weisshaar, T. Mitchell-Olds, *Genetics* **169**, 1601 (2005).
27. R. R. Hudson, N. L. Kaplan, *Genetics* **120**, 831 (1988).
28. M. Nordborg, *Genetics* **146**, 1501 (1997).
29. J. Kroymann, T. Mitchell-Olds, *Nature* **435**, 95 (2005).
30. D. Tian, H. Araki, E. Stahl, J. Bergelson, M. Kreitman, *Proc. Natl. Acad. Sci. U.S.A.* **99**, 11525 (2002).
31. A. L. Hughes, M. Nei, *Nature* **335**, 167 (1988).
32. M. Nordborg, H. Innan, *Genetics* **163**, 1201 (2003).
33. Eightfold coverage for *A. lyrata* and *Capsella rubella* is being generated by the Joint Genome Institute (www.jgi.doe.gov/).
34. N. L. Kaplan, R. R. Hudson, C. H. Langley, *Genetics* **123**, 887 (1989).
35. J. M. Smith, J. Haigh, *Genet. Res.* **23**, 23 (1974).
36. C. Toomajian *et al.*, *PLoS Biol.* **4**, e137 (2006).
37. A. C. Syvanen, *Nat. Genet.* **37** (Suppl.), S5 (2005).
38. M. Morgante, *Curr. Opin. Biotechnol.* **17**, 168 (2006).

39. We thank G. Nielson and H. Huang for bioinformatics support; R. Gupta and M. Morenzoni for information management; T. Altman, J. Borevitz, C. Dean, and C. Shindo for seed stocks; J. Gagne, D. Gingerich, R. Vierstra, L. Sterck, and Y. van de Peer for providing gene family or homology information; and K. Schneeberger for helpful discussions. Supported by Innovation Funds of the Max Planck Society, NIH (HG002790 to M. Waterman, and GM62932 to J. Chory and D.W.), NSF (DEB-0115062 to M.N., and DBI-0520253 to J.R.E.), an NIH National Research Service Award fellowship to C.T., and core funding from the Max Planck Society. D.W. is a director of the Max Planck Institute. Sequence data have been deposited in GenBank (accession codes EI100660 to EI102044).

Supporting Online Material

www.sciencemag.org/cgi/content/full/317/5836/338/DC1
Materials and Methods
Figs. S1 to S20
Tables S1 to S15
References and Notes

11 December 2006; accepted 7 June 2007
10.1126/science.1138632

REPORTS

Imaging the Surface of Altair

John D. Monnier,[1]* M. Zhao,[1] E. Pedretti,[2] N. Thureau,[3] M. Ireland,[4] P. Muirhead,[5] J.-P. Berger,[6] R. Millan-Gabet,[7] G. Van Belle,[7] T. ten Brummelaar,[8] H. McAlister,[8] S. Ridgway,[9] N. Turner,[8] L. Sturmann,[8] J. Sturmann,[8] D. Berger[1]

Spatially resolving the surfaces of nearby stars promises to advance our knowledge of stellar physics. Using optical long-baseline interferometry, we constructed a near-infrared image of the rapidly rotating hot star Altair with a resolution of <1 milliarcsecond. The image clearly reveals the strong effect of gravity darkening on the highly distorted stellar photosphere. Standard models for a uniformly rotating star cannot explain our findings, which appear to result from differential rotation, alternative gravity-darkening laws, or both.

Whereas solar astronomers can take advantage of high-resolution, multiwavelength, real-time imaging of the Sun's surface, stellar astronomers know most stars—whether located parsecs or kiloparsecs away—as simple points of light. To discover and understand the processes around stars unlike the Sun, we must rely on stellar spectra averaged over the entire photosphere. Despite their enormous value, spectra alone have been inadequate to resolve central questions in stellar astronomy, such as the role of angular momentum in stellar evolution (*1*), the production and maintenance of magnetic fields (*2*), the launching of massive stellar winds (*3*), and the interactions between very close binary companions (*4*).

Fortunately, solar astronomers no longer hold a monopoly on stellar imaging. Long-baseline visible and infrared interferometers have enabled the cataloging of photospheric diameters of hundreds of stars and high-precision dynamical masses for dozens of binaries, offering exacting constraints for theories of stellar evolution and stellar atmospheres (*5*). This work requires an angular resolution of ~1 milliarcsecond (mas) (1 part in 2×10^8, or 5 nanoradians) for resolving even nearby stars, which is more than an order of magnitude better than that achievable with the Hubble Space Telescope or ground-based 8-m telescopes equipped with adaptive optics.

Stellar imaging can be used to investigate the rapid rotation of hot, massive stars. A large fraction of hot stars are rapid rotators with surface rotational velocities of more than 100 km/s (*6*, *7*). These rapid rotators are expected to traverse evolutionary paths very different from those of their slowly rotating kin (*1*), and rotation-induced mixing alters stellar abundances (*8*). Although hot stars are relatively rare by number in the Milky Way Galaxy, they have a disproportionate effect on galactic evolution due to their high luminosities, their strong winds, and their final end as supernovae (for the most massive stars). Recently, rapid rotation in single stars has been invoked to explain at least one major type of gamma-ray bursts (*9*) and binary coalescence of massive stars or remnants (*10*).

The distinctive observational signatures of rapid rotation were first described by von Zeipel (*11*), beginning with the expectation that centrifugal forces would distort the photospheric shape and that the resulting oblateness would induce lower effective temperatures at the equator. This latter effect, known as gravity darkening, will cause distortions in the observed line profiles as well as the overall spectral energy distribution. Precise predictions can be made, but these rely on uncertain assumptions, in particular the distribution of angular momentum in the star; uniform rotation is often assumed for simplicity.

The most basic predictions of von Zeipel theory—centrifugal distortion and gravity darkening—have been confirmed to some extent. The Palomar Testbed Interferometer (PTI), the first instrument to measure photospheric elongation in a rapid rotator, found the diameter of the nearby A-type star Altair to be ~14% larger in one dimension than the other (*12*). The Navy Prototype Optical Interferometer (NPOI) and the Center for High Angular Resolution Astronomy (CHARA) interferometric array both measured strong limb-darkening profiles for the photometric standard Vega (*13*, *14*), consistent with a rapid rotator viewed nearly pole-on. A brightness asymmetry for Altair was also reported by NPOI (*15*, *16*), suggestive of the expected pole-to-equator temperature difference from gravity darkening. In recent years, a total of five rapid rotators have been measured to be elongated by interferometers (*17*–*19*).

Although von Zeipel theory appears to work at a basic level, serious discrepancies between theory and observations have emerged. Most notably, the diameter of the B3V-type star Achernar (*17*) was measured to be ~56% longer in one dimension than the other, a discrepancy too large to be explained by von Zeipel theory. Explanations for this include strong differential rotation of the star (*20*) or the presence of a polar wind (*3*), either of which have far-reaching consequences for our understanding of stellar evolution. To address these issues, we must move beyond the simplest models for rapidly rotating stars, and this will require a corresponding jump in the quality and quantity of interferometry data. Indeed, all previous results were based on limited interferometer baselines that lacked the capability to form model-independent images, and relied entirely on model fitting for interpretation. Thus, previous confirmations of von Zeipel theory, although suggestive, were incomplete.

Here we report a development in imaging capabilities that enables a test of von Zeipel theory, both through basic imaging and precise model-fitting. By combining near-infrared light from four telescopes of the CHARA interferometric array, we have synthesized an elliptical aperture with dimensions 265 m by 195 m (Fig. 1), allowing us to reconstruct images of the prototypical rapid rotator Altair (spectral type A7V) with an angular resolution of ~0.64 mas, the diffraction limit defined by $\lambda/2D$, the observing wavelength divided by twice the longest interferometer baseline. The recently commissioned Michigan Infrared Combiner (MIRC) (*21*) was essential for this work, allowing the light from the CHARA telescopes to be combined simultaneously into eight spectral channels spanning the astronomical H band

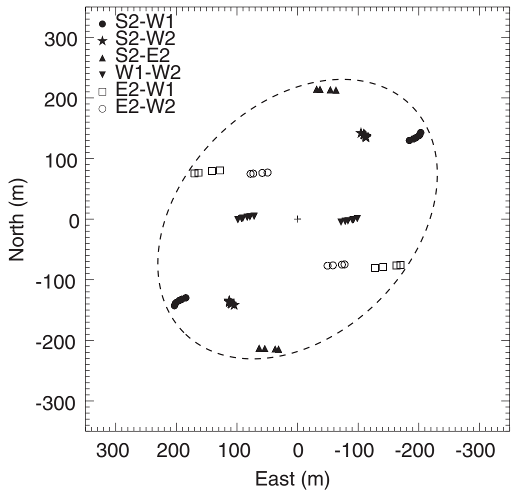

Fig. 1. Fourier (*u*, *v*) coverage for the Altair observations, where each point represents the projected separation between one pair of the four CHARA telescopes S2, E2, W1, and W2 (*31*). The dashed ellipse shows the equivalent coverage for an elliptical aperture of 265 m by 195 m oriented along a position angle of 135° east of north.

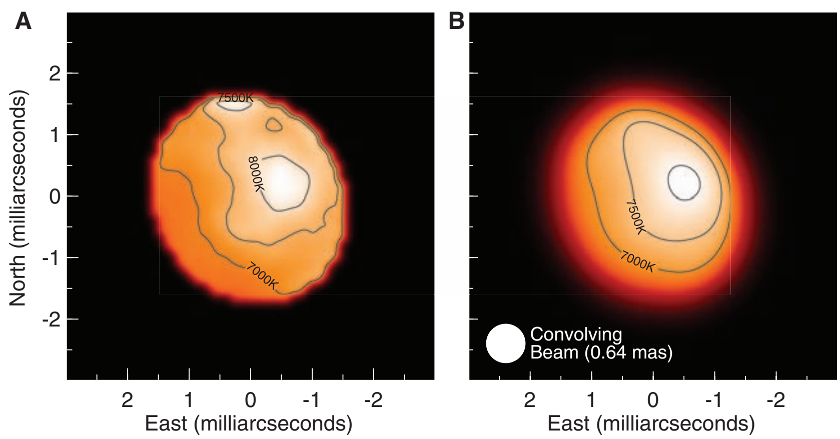

Fig. 2. (**A**) Intensity image of the surface of Altair (λ = 1.65 μm) created with the MACIM/MEM imaging method using a uniform brightness elliptical prior (χ^2_ν= 0.98). Typical photometric errors in the image correspond to ±4% in intensity. (**B**) Reconstructed image convolved with a Gaussian beam of 0.64 mas, corresponding to the diffraction limit of CHARA for these observations. For both panels, the specific intensities at 1.65 μm were converted into the corresponding blackbody temperatures; contours for 7000, 7500, and 8000 K are shown. North is up and east is left.

[1]Department of Astronomy, University of Michigan, Ann Arbor, MI 48109, USA. [2]School of Physics and Astronomy, University of St. Andrews, Fife KY16 9AJ, Scotland, UK. [3]Astrophysics Group, Cavendish Laboratory, Cambridge University, Cambridge CB3 0HA, UK. [4]Division of Geological and Planetary Sciences, California Institute of Technology, Pasadena, CA 91125, USA. [5]Astronomy Department, Cornell University, Ithaca, NY 14850, USA. [6]Laboratoire d'Astrophysique de Grenoble, Observatoire de Grenoble, F-38041 Grenoble Cédex 9, France. [7]Michelson Science Center, California Institute of Technology, Pasadena, CA 91125, USA. [8]Center for High Angular Resolution Astronomy, Georgia State University, Atlanta, GA 30302, USA. [9]National Optical Astronomy Observatory, Tucson, AZ 85719, USA.

*To whom correspondence should be addressed. E-mail: monnier@umich.edu

(λ = 1.50 to 1.74 μm). The Altair data presented here were collected on 31 August and 1 September 2006 (UT); complete observational information is available (*22*). In addition, we used some K-band (λ = 2.2 μm) observations by the PTI to constrain the short-baseline visibilities in subsequent analysis.

With the use of four CHARA telescopes, interferometric imaging of Altair is now possible, although this requires specialized image reconstruction techniques. We used the publicly available application MACIM (Markov-Chain Imager for Optical Interferometry) (*23*) in this work, applying the maximum entropy method (MEM) (*24*). We restricted the stellar image to fall within an elliptical boundary, similar in principle to limiting the field of view in standard aperture synthesis procedures. This restriction biases our imaging against faint emission features arising outside the photosphere; however, we do not expect any circumstellar emission in Altair, which is relatively cool, lacking signs of gas emission or strong winds. Further details of our imaging procedures, along with results from validation tests, can be found in (*22*). Our image shows the stellar photosphere of Altair to be well resolved (Fig. 2A), appearing elongated in the northeast-southwest direction with a bright dominant feature covering the northwest quadrant of the star. To reduce the influence of possible low-level artifacts that are beyond the diffraction limit of our interferometer, we have followed the standard procedure (*25*) of convolving the reconstructed image with a Gaussian beam matching the resolution of the interferometer (Fig. 2B).

These images confirm the basic picture of gravity darkening induced by rapid rotation. We see Altair's photosphere to be oblate with a bright region identifiable as the stellar polar region. The intensity of the dark equatorial band is about 60 to 70% of the brightness at the pole, broadly consistent with expectations for the near-infrared from previous models. Although we see some evidence for deviations from axisymmetry (small excess emission on the northern limb), this feature is at the limit of our image fidelity and will require additional Fourier coverage to investigate further. We have also fitted our data set with a rapid rotator model, following the prescription set out in Aufdenberg *et al.* (*14*) and references therein, assuming a Roche potential (central point mass) and solid-body rotation. The main parameters of the model are the stellar radius and temperature at the pole, the angular rotation rate as a fraction of breakup (ω), the gravity darkening coefficient (β), and the viewing angles (inclination and position angle). We used the stellar atmosphere models of Kurucz (*26*) to determine the specific intensity of each point on the surface as a function of local gravity, effective temperature, and limb darkening. In addition to matching the new MIRC/CHARA data, we forced the model to match the measured V- and H-band photometric magnitudes (0.765 ± 0.015 and 0.235 ± 0.043, respectively) derived from a broad literature survey. When fixing the gravity-darkening coefficient to β = 0.25 appropriate for radiative envelopes, our derived parameters (Table 1) agree well with the best-fit parameters of Peterson *et al.* (*15*) on the basis of visible data. However, our best-fit model reached only a reduced χ^2_ν of 1.79, which suggests a need for additional degrees of freedom in our model. To improve our fits, we explored an extension to the von Zeipel model, allowing the gravity-darkening coefficient β to be a free parameter. We found that a model with β = 0.190 significantly improved the goodness of fit (Table 1), and this improvement is visually apparent when comparing synthetic model images to the Altair image from CHARA (Fig. 3). In addition to a lower β, the new model prefers a slightly less inclined orientation, a cooler polar temperature, and a faster rotation rate.

Both our imaging and modeling results point to important deficiencies in the currently popular models for rapid rotators. Previous workers have also encountered problems explaining high-resolution interferometry data with standard prescriptions for rotating stars. In addition to the Achernar case previously cited, Peterson *et al.* (*15*) were unable to find a satisfactory fit for Altair assuming a standard Roche–von Zeipel model (χ^2_ν = 3.8), consistent with the need for additional stellar physics. Recent results for Alderamin (*19*) also specifically favor models with smaller βs, in line with our findings. Although model fitting has revealed deviations from standard theory, our model-independent imaging allows new features to be discovered outside current model paradigms. The most striking difference between our CHARA image and the synthetic model images (Fig. 3) is that our image shows stronger darkening along the equator, inconsistent with any von Zeipel–like gravity-darkening prescription assuming uniform

Table 1. Best-fit parameters for Roche–von Zeipel models of Altair. Parameter descriptions: Inclination (0° is pole-on, 90° is edge-on) and position angle (degrees east of north) describe our viewing angle, T_{pole} and R_{pole} describe the temperature and radii of the pole (alternatively, one can describe the temperature and radii at the equator as T_{eq} and R_{eq}), ω is the angular rotation rate as a fraction of critical breakup rate, and β is the gravity-darkening coefficient. Models assumed stellar mass = 1.791 $M_\odot$ (*15*), metallicity [Fe/H] = –0.2 (*32*), and distance = 5.14 pc (*33*).

Parameter	β fixed	β free
Inclination	62.7° ± 1.5°	57.2° ± 1.9°
Position angle	–61.7° ± 0.9°	–61.8° ± 0.8°
T_{pole} (K)	8710 ± 160	8450 ± 140
R_{pole} ($R_\odot$)	1.661 ± 0.004	1.634 ± 0.011
(mas)	1.503 ± 0.004	1.479 ± 0.010
T_{eq} (K)	6850 ± 120	6860 ± 150
R_{eq} ($R_\odot$)	2.022 ± 0.009	2.029 ± 0.007
(mas)	1.830 ± 0.008	1.835 ± 0.007
ω	0.902 ± 0.005	0.923 ± 0.006
β	0.25 (Fixed)	0.190 ± 0.012
Model V-band photometric magnitude	0.765	0.765
Model H-band photometric magnitude	0.225	0.220
Model *v* sin *i* (km/s)	241	240
Reduced χ^2:		
Total	1.79	1.37
Closure phase	2.08	1.73
Vis^2	1.48	1.10
Triple amp	2.14	1.58

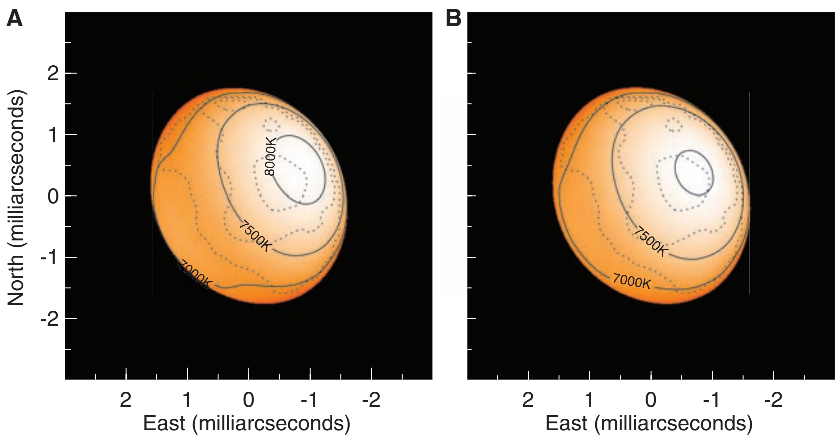

Fig. 3. Synthetic images of Altair (λ = 1.65 μm) adopting conventional rapid-rotation models. (**A**) The best-fit model assuming standard gravity-darkening coefficient for radiative envelopes (β = 0.25, χ^2_ν = 1.79). (**B**) The result when β is a free parameter (β = 0.190, χ^2_ν = 1.37). For both panels, the specific intensities at 1.65 μm were converted into the corresponding blackbody temperatures; contours for 7000, 7500, and 8000 K are shown. We have overplotted the contours from the CHARA image (Fig. 2A) as dotted lines to facilitate intercomparison.

rotation. Lower equatorial surface temperatures could naturally arise if the equatorial rotation rate were higher than the rest of the star (differential rotation), reducing the effective gravity at the surface (*27*). Another possibility is that the cooler equatorial layers could be unstable to convection (*28*, *29*), invalidating a single gravity-darkening "law" applicable to all stellar latitudes. Other studies (*30*) have found further faults with simple application of the von Zeipel law due to opacity effects in the surface layers. Even though it is difficult to isolate or untangle these various effects from one another, the new interferometric results and our modeling convincingly establish the case for stellar physics beyond the standard models used today to describe rotating stars. A path forward is clear: Differential rotation will leave both geometric and kinematic signatures different from opacity or convection-related phenomena. Observers must be armed with a new generation of models incorporating these physical processes in order to exploit the powerful combination of detailed line profile analysis and multiwavelength interferometric imaging now available.

References and Notes

1. A. Maeder, G. Meynet, *Annu. Rev. Astron. Astrophys.* **38**, 143 (2000).
2. J. D. Landstreet, *Astron. Astrophys. Rev.* **4**, 35 (1992).
3. P. Kervella, A. Domiciano de Souza, *Astron. Astrophys.* **453**, 1059 (2006).
4. P. Barai *et al.*, *Astrophys. J.* **608**, 989 (2004).
5. J. D. Monnier, *Rep. Prog. Phys.* **66**, 789 (2003).
6. H. A. Abt, N. I. Morrell, *Astrophys. J. Suppl. Ser.* **99**, 135 (1995).
7. H. A. Abt, H. Levato, M. Grosso, *Astrophys. J.* **573**, 359 (2002).
8. M. Pinsonneault, *Annu. Rev. Astron. Astrophys.* **35**, 557 (1997).
9. G. E. Brown *et al.*, *N. Astron.* **5**, 191 (2000).
10. N. Gehrels *et al.*, *Nature* **437**, 851 (2005).
11. H. von Zeipel, *Mon. Not. R. Astron. Soc.* **84**, 684 (1924).
12. G. T. van Belle, D. R. Ciardi, R. R. Thompson, R. L. Akeson, E. A. Lada, *Astrophys. J.* **559**, 1155 (2001).
13. D. M. Peterson *et al.*, *Nature* **440**, 896 (2006).
14. J. P. Aufdenberg *et al.*, *Astrophys. J.* **645**, 664 (2006).
15. D. M. Peterson *et al.*, *Astrophys. J.* **636**, 1087 (2006).
16. N. Ohishi, T. E. Nordgren, D. J. Hutter, *Astrophys. J.* **612**, 463 (2004).
17. A. Domiciano de Souza *et al.*, *Astron. Astrophys.* **407**, L47 (2003).
18. H. A. McAlister *et al.*, *Astrophys. J.* **628**, 439 (2005).
19. G. T. van Belle *et al.*, *Astrophys. J.* **637**, 494 (2006).
20. S. Jackson, K. B. MacGregor, A. Skumanich, *Astrophys. J.* **606**, 1196 (2004).
21. J. D. Monnier, J.-P. Berger, R. Millan-Gabet, T. A. Ten Brummelaar, *Proc. SPIE* **5491**, 1370 (2004).
22. See supporting material on *Science* Online.
23. M. J. Ireland, J. D. Monnier, N. Thureau, *Proc. SPIE* **6268**, 62681T (2006).
24. R. Narayan, R. Nityananda, *Annu. Rev. Astron. Astrophys.* **24**, 127 (1986).
25. J. A. Högbom, *Astron. Astrophys.* **15** (suppl.), 417 (1974).
26. R. Kurucz, *ATLAS9 Stellar Atmosphere Programs and 2 km/s Grid* (Smithsonian Astrophysical Observatory, Cambridge, MA, 1993).
27. S. Jackson, K. B. MacGregor, A. Skumanich, *Astrophys. J. Suppl. Ser.* **156**, 245 (2005).
28. A. Claret, *Astron. Astrophys.* **359**, 289 (2000).
29. F. Espinosa Lara, M. Rieutord, http://arxiv.org/abs/astro-ph/0702255 (2007).
30. C. Lovekin, R. G. Deupree, C. I. Short, *Astrophys. J. Suppl. Ser.* **643**, 460 (2006).
31. T. A. ten Brummelaar *et al.*, *Astrophys. J.* **628**, 453 (2005).
32. D. Erspamer, P. North, *Astron. Astrophys.* **398**, 1121 (2003).
33. European Space Agency, *The Hipparcos and Tycho Catalogues* (1997) (www.rssd.esa.int/Hipparcos/catalog.html).

34. We thank A. Tannirkulam, S. Webster, A. Boden, B. Zavala, C. Tycner, C. Hummel, D. Peterson, J. Aufdenberg, PJ Goldfinger, and S. Golden for their contributions. Research at the CHARA Array is supported by NSF grants AST 06-06958 and AST 03-52723 and by the offices of the Dean of the College of the Arts and Sciences and the Vice President for Research, Georgia State University.

Supporting Online Material

www.sciencemag.org/cgi/content/full/1143205/DC1
Materials and Methods
Figs. S1 to S5
References

29 March 2007; accepted 23 May 2007
Published online 31 May 2007;
10.1126/science.1143205
Include this information when citing this paper.

The Crystallization Age of Eucrite Zircon

G. Srinivasan,[1]* M. J. Whitehouse,[2] I. Weber,[3] A. Yamaguchi[4]

Eucrites are a group of meteorites that represent the first planetary igneous activity following metal-silicate differentiation on an early planetesimal, similar to Asteroid 4 Vesta, and, thus, help date geophysical processes occurring on such bodies in the early solar system. Using the short-lived radionuclide ^{182}Hf as a relative chronometer, we demonstrate that eucrite zircon crystallized quickly within 6.8 million years of metal-silicate differentiation. This implies that mantle differentiation on the eucrite parent body occurred during a period when internal heat from the decay of ^{26}Al and ^{60}Fe was still available. Later metamorphism of eucrites took place at least 8.9 million years after the zircons crystallized and was likely caused by heating from impacts, or by burial under hot material excavated by impacts, rather than from lava flows. Thus, the timing of eucrite formation and of mantle differentiation is constrained.

The accretion of the parent bodies of differentiated meteorites (e.g., eucrites), Mars, Moon, and Earth was quickly followed by large-scale melting and metal-silicate differentiation, resulting in core-mantle formation. Basaltic eucrites are a group of differentiated meteorites that formed as lava flows or as shallow intrusions following metal-silicate differentiation on the eucrite parent body (EPB). Asteroid 4 Vesta is identified as a plausible eucrite parent body (*1*). Time constraints on the processes of melting, metal-silicate separation leading to core formation, and subsequent mantle differentiation that produced precursors to basaltic eucrites are critical to models of the thermal evolution of EPB. To constrain precisely the time of eruption and crystallization of basalts on EPB, we report high-precision measurements of the Hf-W composition of zircon from three eucrites and explore the use of ^{182}Hf as a relative chronometer.

Eucrites are composed primarily of pyroxene; plagioclase; minor chromite; ilmenite; and trace quantities of zircon, metal, and quartz. The presence of decay products of short-lived radionuclides, ^{26}Al [half-life ($T_{1/2}$) ≈ 0.7 million years (My)], ^{53}Mn ($T_{1/2}$ ≈ 3.5 My) and ^{182}Hf ($T_{1/2}$ ≈ 8.9 My) (*2*–*5*), in eucrites requires their formation within a few million years of formation of the solar system. An age of 4555 ± 9 My is inferred from the ^{207}Pb/^{206}Pb composition of eucrite zircons (*6*). This age spans the entire time window when the eucrite parent body (EPB) was undergoing extensive igneous activity fuelled by heat produced from the decay of short-lived radionuclides ^{26}Al and ^{60}Fe ($T_{1/2}$ ≈ 1.5 My).

Eucrites are extensively metamorphosed and extremely brecciated as a result of impacts. Related thermal disturbance of parent-daughter isotopic systematics of radiometric chronometers can potentially obscure crystallization records. Therefore, the eucrite crystallization ages determined from long-lived chronometers, e.g., ^{147}Sm ($T_{1/2}$ ≈ 103 Gy) and short-lived chronometers (e.g., ^{26}Al) are poorly constrained (*7*), as are models of the thermal evolution of EPB.

When planets containing bulk solar proportions of elements are melted and differentiated, lithophile Hf and siderophile W are chemically fractionated and redistributed into the silicate mantle and metallic core, respectively (*8*). Therefore, the decay of ^{182}Hf to ^{182}W has been used to determine time scales of metal-silicate differentiation leading to core formation of planets (*5*) and mantle differentiation resulting in eruption of basalts on EPB (*4*, *5*). However, Hf-W compositions of bulk silicate mineral and metal separates in eucrites reflect meta-

[1]Department of Geology, University of Toronto, Toronto, ON, Canada, M5S 3B1. [2]Laboratory for Isotope Geology, Swedish Museum of Natural History, SE-104 05 Stockholm, Sweden. [3]Institute for Planetology, Department of Geosciences, University of Münster, D-48149 Münster, Germany. [4]National Institute of Polar Research, Tokyo 173-8515, Japan.

*To whom correspondence should be addressed. E-mail: srini@geology.utoronto.ca